Correlation-induced *d*-wave pairing in a quantum dot square lattice

A. Biborski ●,* M. P. Nowak ●,† and M. Zegrodnik ●‡

AGH University of Science and Technology, Academic Centre for Materials and Nanotechnology, Al. Mickiewicza 30, 30-059 Krakow, Poland

We consider an electrostatically induced square lattice of quantum dots and study the role of electron-electron correlations in the resulting electronic features of the system. We utilize the Wannier functions methodology to construct a Hamiltonian for interacting fermions, and find that the change of the depth of the quantum dot confining potential results in a transition from a moderately, to strongly correlated regime of the system. We obtain the approximate ground state by means of the variational Monte Carlo method for a wide range of dopings. The values of microscopic parameters, charge gap, as well as spin- and pair-correlation functions obtained in the strongly correlated regime signify the presence of antiferromagnetic spin ordering and the realization of the Mott insulator phase. Moreover, we report on a two-dome structure of the emerging *d*-wave paired state residing on both sides of the half-filled case. The obtained results are discussed in view of the well-known family of unconventional superconducting materials, such as copper-based compounds.

I. INTRODUCTION

Unconventional phases which appear in the correlated electron systems have gathered a significant amount of interest over the years. At low energies, correlated materials show conflicting tendencies towards different symmetry-broken states leading to complex phase diagrams and exotic physical properties, such as unconventional forms of superconductivity, magnetism, non-Fermi liquid behavior, and Mott physics [1]. In spite of extensive experimental and theoretical effort, the complete theoretical description of many prominent examples of correlated system, such as cuprates [2,3] or heavy-fermion materials [4], still remains unclear. One of the main issues in formulating the proper theoretical approach is related to incorporating the electron-electron interaction with satisfactory precision. Calculation methods dedicated to correlated systems are characterized by a high degree of complexity, which limits their applicability only to simplified models and/or systems with a significantly reduced size. In this respect, the seminal Hubbard [1,5,6] and *t-J* [1,7] models or their derivatives are usually considered as candidates which can allow clarifying the nature of the strongly correlated phenomena.

At the same time, novel correlated systems are being discovered, which can allow for better experimental verification of the proposed theoretical concepts. It is believed that the recently synthesized twisted bilayer graphene [8,9], due to its high degree of tunability, will allow answering open questions related to the interacting electron phenomena. The major advantage of twisted bilayer graphene with respect to the previously known correlated systems is that the electron

density can be easily tuned by using electronic gates, thus avoiding the disruptive effects of chemical doping. Moreover, the strength of correlations can be controlled by changing the twist angle. Another system in which many microscopic parameters can be controlled experimentally consists of ultracold atoms trapped in an optical lattice [10,11]. In spite of the fact that such a system has been discovered already some time ago, it is still considered as one of the most promising experimental setups to simulate the behavior of the Hubbard model.

Furthermore, the electronic correlations may also play an important role in the physics of nanoscopic systems. Specifically, quantum dots (QDs) are often considered as artificial atoms [12] and can be regarded as building blocks for more complex devices in which the precise inclusion of electron-electron interactions is indispensable for proper description. Here, we consider the use of QDs as a route to realize highly tunable, strongly correlated electron systems. The advancement in nanofabrication methods allows for the creation of electrostatically controlled QDs [13], as well as their patterns in two dimensions [14–16]. By proper architecture of gates, such a pattern of QDs can serve as an experimental realization of the two-dimensional Hubbard model with both the electron concentration and strength of correlations controlled *in situ* by means of gate voltage [17,18]. This provides an opportunity to clarify many of the long-standing problems related to emergent phenomena in interacting electron systems.

In this theoretical analysis, we elucidate the phenomena arising from electron-electron interactions by considering a square lattice consisting of electrostatically fabricated dots and use variational Monte Carlo (VMC) method to capture the correlation effects. We start from an approach complementary with respect to the previously performed studies [17,18], i.e., we use the real-space picture, and consequently build a translationally invariant system. Notably, we take into account the

*andrzej.biborski@agh.edu.pl
†mpnowak@agh.edu.pl
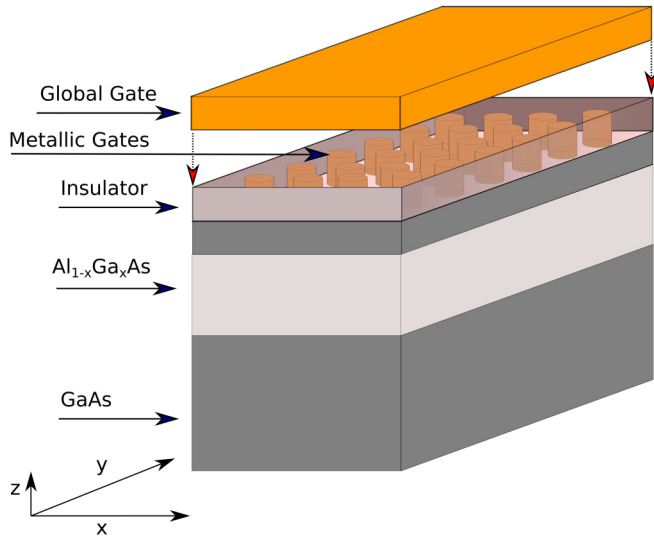‡michal.zegrodnik@agh.edu.pl

FIG. 1. Schematic representation of the considered structure. Note that space between the insulator layer and the global gate is only for presentation purposes.

screening effects resulting from the proximity of the metallic top gate, which is important to reduce the amplitude of two-body interactions [17] as pointed out by Byrnes *et al.* Our main finding is that the QDs' lattice realizes the correlation-driven antiferromagnetic ordering, Mott-insulating phase, and most importantly *d*-wave superconductivity. So far, the presumption of the existence of *d*-wave superconductivity in such systems has been made only based on the relation between values of interaction amplitudes and the single-particle spectrum for the effective interacting models describing QDs lattice [17]. In this work *we inspect explicitly* if such a scenario takes place and provide theoretical evidence of pairing in the *d*-wave channel for the low-carrier density (implicitly assumed by considering only the lowest band) and within general interacting Hamiltonian. The obtained results are discussed in view of the well-known families of unconventional superconducting materials such as cuprates.

In the next section, we describe the model of the QD layer. Subsequently, the section devoted to the methodology covers both the construction of Wannier basis and the calculation of transfer (hopping) and interaction integrals, as well as the solution of many-body Hamiltonian in terms of VMC method. In Sec. III, we present the results obtained for the selected lattice spacing and different depths of the confining potential V^C. We discuss the electronic properties of the system for the selected confinement as a function of charge doping (carrier density) in terms of the analysis of one- and two-body correlation functions, discussing the spin order and the development of charge-gap, as well as the evidence of singlet pairing. Finally, we summarize the obtained results and conclude in the very last section.

II. MODEL

We follow the concept of the device presented by Byrnes *et al.* [17], based on GaAs/AlGaAs-layered heterostructure (Fig. 1) in which a two-dimensional electron gas (2DEG) is formed. The top global gate controls the electron concentration in the system, whereas the metallic electrodes, assembled as a square lattice pattern, are immersed in an insulator layer allowing for modulation of the periodic confinement. In this manner, both doping and electron confinement are tunable, allowing us to switch between diverse regimes characterized by different strengths of the electronic correlation as well as scan the resulting phase diagram.

Here, instead of considering the globally assumed periodic potential [17], we start from the single-particle spectrum of the isolated QD. A variety of confinement potentials V^{QD} have been exploited to realistically model the electrostatically induced QD [19,20], e.g., parabolic, Gaussian, power exponential. We restrict our choice to the form which exhibits radial symmetry in the $\hat{\mathbf{x}} - \hat{\mathbf{y}}$ plane, as well as, is spatially convergent, i.e., $\lim_{\mathbf{r} \to \infty} V^{QD}(\mathbf{r} - \mathbf{R}) = \text{const.}$, where $\mathbf{r} = (x, y)$ and $\mathbf{R}$ refers to the V^{QD} center. The explicit form of the exploited Gaussian potential for QD is given as

$$V_{\mathbf{R}}^{QD}(\mathbf{r}) = V_0 \times \exp\left[-\left(\frac{||\mathbf{r} - \mathbf{R}||}{r_0} \right)^2 \right], \qquad (1)$$

where V_0 tunes quantum well depth and r_0 controls its planar size. The Gaussian form of $V_{\mathbf{R}}^{QD}$ is believed to describe properly the shape of potential for GaAs-based devices for the relatively small electrode radius (less than 10^2 nm), which in our case is also very close to the value of r_0 [19]. The planar confinement V^C originating from the whole pattern of electrodes has the form

$$V_a^C(\mathbf{r}) = V_0 - \sum_i \sum_j V_{\mathbf{R}_{ij}}^{QD}(\mathbf{r}), \qquad (2)$$

where a is the lattice spacing and $\mathbf{R}_{ij} = (i \times a\hat{\mathbf{x}}, j \times a\hat{\mathbf{y}})$. Note that, when a is sufficiently larger than r_0, this parametrization leads to $V_a^C(i \times a\hat{\mathbf{x}}, j \times a\hat{\mathbf{y}}) \approx 0$ and $V_a^C(\frac{i}{2} \times a\hat{\mathbf{x}}, \frac{j}{2} \times a\hat{\mathbf{y}}) \approx V_0$.

III. METHOD

We employ the following stages in the computational procedure: (i) Schrödinger equation solution for assumed V^{QD}; (ii) Wannier basis construction; (iii) formulation of many body Hamiltonian; (iv) VMC solution of the interacting system. We briefly describe each stage in the following subsections.

A. Spectrum of an isolated QD

According to the form of the confining potential adapted here [Eq. (1)], the single QD is parametrized by $\{V_0, r_0\}$. Analytical solution of the Schrödinger equation for the radially symmetrical power-exponential potential is not known [20], thus single-particle eigenequation needs to be diagonalized numerically. As the aforementioned form of the potential exhibits radial symmetry, the time-independent Schrödinger equation can be factorized in a regular manner, i.e., as a product of the radial and angular parts, namely,

$$\Theta_{nl}(r, \phi) = R_{nl}(r) \Phi_l(\phi). \qquad (3)$$

The angular part $R_{nl}(r)$ is the solution of the equation

$$\left[r^2 \frac{\partial^2}{\partial r^2} + r \frac{\partial}{\partial r} + r^2 \frac{2m^*}{\hbar^2} [E_{nl} - V(r)] - \frac{l^2}{\hbar^2} \right] R_{nl}(r) = 0, \quad (4)$$

and $\Phi_l(\phi)$ is given as

$$\Phi_l(\phi) = \exp\left(i \frac{l}{\hbar} \phi \right), \quad (5)$$

where $n = 0, 1, 2, \ldots; l = 0, \pm 1, \pm 2 \ldots$ are the principal and angular quantum numbers, respectively. We set $m^* = 0.067 m_e$, i.e., the value of effective mass for GaAs. Equation (4) can be transformed to the form of an eigenproblem for a given value of l^2, which can be efficiently solved within the numerical scheme recently proposed by Laliena and Campo [21], as we implemented in our code.

B. Wannier basis

The electron wave function in the lattice of QDs can be defined in the basis of Wannier functions constructed with the use of the previously specified $\{\Theta_{nl}(r, \phi)\}$ functions. Although neither l nor n are good quantum numbers for the finite lattice spacing a, we apply them for indexing also in the resulting Wannier functions. Namely, they are defined as a linear combination of $\Theta_{nl}(r, \phi)$ as

$$w_{nl}^{R_{ij}}(\mathbf{r}) \equiv \sum_{n',l'} \sum_{\mathbf{r_Z}} \alpha_{r_Z, n', l'} \Theta_{n'l'}(\mathbf{r} - \mathbf{R_{ij}} + \mathbf{r_Z}), \quad (6)$$

where the $\lim_{a \to \infty} w_{nl}^{R_{ij}}(\mathbf{r}) = \Theta_{nl}(\mathbf{r} - \mathbf{R_{ij}})$ condition defines the values of n, l for the elements of the Wannier basis. The coefficients $\{\alpha_{r_Z, n, l}\}$ are to be determined where $\mathbf{r_Z}$ are vectors pointing to Zth nearest-neighboring lattice site. A finite number of orbitals are taken into account to perform numerical orthogonalization of Wannier functions. Therefore, we consider only those Θ_{nl} for which $E_{n,l} < V_0$ in the expansion in Eq. (6). This basis truncation is adequate when a is sufficiently large in comparison to r_0, i.e., when the application of the Wannier wave functions is justified. Also, we take into account a finite number of neighboring sites, and consider a finite, square cluster of size $2m + 1 \times 2m + 1$. Next $\alpha_{r_Z, n', l'}$ are obtained by means of Löwdin orthogonalization [22]. When m is systematically increased, central [i.e., those centered at $\mathbf{R}_{mm} = (m \times a, m \times a)$] Wannier functions may be treated as transitionally invariant within the desired numerical precision [23].

We assume an infinite quantum well confinement in the $\hat{\mathbf{z}}$ direction. Therefore, we formulate the final form of a single-particle wave function as a product of $w_{nl}^{R_{ij}}(\mathbf{r})$ and the ground state of the confinement in the direction perpendicular to the lattice, namely,

$$\widetilde{w}_{nl}^{R_{ij}}(\mathbf{r}, z) = w_{nl}^{R_{ij}}(\mathbf{r}) \sqrt{\frac{2}{L}} \cos\left(\frac{\pi z}{L} \right), \quad (7)$$

where we take $L = 10$ nm—which is a reasonable value for 2DEG quantum well width [24]. Eventually, we have

$$\left\langle \widetilde{w}_{nl}^{R_{ij}}(\mathbf{r}, z) \middle| \widetilde{w}_{n'l'}^{R_{pq}}(\mathbf{r}, z) \right\rangle \approx \delta_{R_{ij}, R_{pq}} \delta_{nl, n'l'}. \quad (8)$$

The above approximation becomes exact for $m \to \infty$. For the localized system, with a relatively small value of m (i.e., $m < 10$) a nearly (limited by the numerical precision) exact fulfillment of the orthogonality relation occurs, as will be shown further on.

C. Many-body Hamiltonian

In the following, we employ the description of the interacting electron system by means of the second quantization formalism. For the sake of clarity, we map R_{ij} positions to lattice site indices, labeled by $\{i, j, k, l\}$, and (l, n) to a single band index $\{\mu, \nu, \gamma, \tau\}$. The full electronic Hamiltonian is given by

$$\hat{\mathcal{H}} = \sum_{i,\mu,\sigma} \epsilon_i^\mu \hat{c}_{i,\mu,\sigma}^\dagger \hat{c}_{i,\mu,\sigma} + \sum_{i,j} \sum_{\mu,\nu} \sum_\sigma t_{ij}^{\mu\nu} \hat{c}_{i,\mu,\sigma}^\dagger \hat{c}_{j,\nu,\sigma}$$
$$+ \frac{1}{2} \sum_{\substack{i,j, \\ k,l}} \sum_{\substack{\mu,\nu, \\ \gamma,\tau}} \sum_{\sigma,\sigma'} V_{ijkl}^{\mu\nu\gamma\tau} \hat{c}_{i,\mu,\sigma}^\dagger \hat{c}_{j,\nu,\sigma'}^\dagger \hat{c}_{l,\tau,\sigma'} \hat{c}_{k,\gamma,\sigma}, \quad (9)$$

where $\hat{c}_{i\mu,\sigma}^\dagger$ ($\hat{c}_{i,\mu,\sigma}$) are the fermionic creation (annihilation) operators for particles with $\sigma = \{\uparrow, \downarrow\}$. The single-particle amplitudes $\{\epsilon_{i\mu}, t_{ij}^{\mu\nu}\}$, as well as two-body $V_{ijkl}^{\mu\nu\gamma\tau}$ interactions are to be determined by means of calculating the following matrix elements:

$$t_{ij}^{\mu\nu} = \langle w_\mu^i(\mathbf{r}) | - \frac{\hbar^2}{2m^*} \nabla_r^2 + V_a^C(\mathbf{r}) | w_\nu^j(\mathbf{r}) \rangle, \quad (10)$$

where we intentionally disregard the integration with respect to z since, for a given $\{V_0, r_0, L, d\}$, this only shifts the diagonal elements (i.e., $t_{ii}^{\mu\mu} = \epsilon_i^\mu$) by a constant value $\hbar^2 \pi^2 / 2m^* L^2$.

The two-body interaction terms take the form [17,23,25,26]

$$V_{ijkl}^{\mu\nu\gamma\tau} = \langle \widetilde{w}_\mu^i(\mathbf{r}, z) \widetilde{w}_\nu^j(\mathbf{r}', z') | \hat{V}_{e-e} | \widetilde{w}_\gamma^k(\mathbf{r}, z) \widetilde{w}_\tau^l(\mathbf{r}', z') \rangle. \quad (11)$$

Note that for the considered system the electrostatic screening resulting from the metallic gates should be included [17] that leads to the following form of the electron-electron interaction, V_{e-e}:

$$\hat{V}_{e-e}(\mathbf{r}, \mathbf{r}', z, z') = \frac{e^2 f(\mathbf{r}, \mathbf{r}', z, z')}{4\pi \varepsilon_0 \varepsilon \sqrt{|\mathbf{r} - \mathbf{r}'|^2 + (z - z')^2}}, \quad (12)$$

where

$$f(\mathbf{r}, \mathbf{r}', z, z') = 1 - \frac{\sqrt{|\mathbf{r} - \mathbf{r}'|^2 + (z - z')^2}}{\sqrt{|\mathbf{r} - \mathbf{r}'|^2 + (z + z' + 2d)^2}} \quad (13)$$

is the screening function and $\varepsilon = 12.9$ is the dielectric constant.

It should be emphasized that $\mathcal{H}$ in Eq. (9) is given in a general form since the quantitative relations among the magnitudes of microscopic parameters are not known *a priori*. However, the number of terms in the Hamiltonian may be reduced by *a posteriori* analysis, i.e., after obtaining integrals for the considered system parametrization, one may exclude the subset of terms in the Hamiltonian, based on the observation of a marginal value (i.e., close to the numerical precision) of the corresponding microscopic amplitudes.

D. Variational Monte Carlo

We employ the VMC method [27,28] to find the approximate ground state of the interacting system. The absence of the infamous sign problem as well as the relatively high numerical efficiency together with the opportunity to exploit flexible variational ansatzes make this approach very useful for a wide class of fermionic systems for which the consistent inclusion of electronic correlation [27] is indispensable. Particularly, fermionic lattice models formulated in the second quantization language can be treated efficiently [23,29–33] in the framework of VMC.

The choice of many-body variational ansatz $|\Psi_T\rangle$ is crucial for the valid determination of the ground-state properties in VMC. Typically, $|\Psi_T\rangle$ is given as the state resulting from acting of the correlation factor $\hat{\mathcal{P}}$ and the projection operator $\hat{\mathcal{L}}$ on the so-called noninteracting wave function $|\Psi_0\rangle$

$$|\Psi_T\rangle = \hat{\mathcal{P}}\hat{\mathcal{L}}|\Psi_0\rangle. \tag{14}$$

One of the possible forms of $|\Psi_0\rangle$ is the pair-product or Pfaffian wave function [27,34] given as

$$|\Psi_0\rangle = \Big[\sum_{i,j}\sum_{\mu\nu}\sum_{\sigma,\sigma'}F_{i\mu,j\nu}^{\sigma\sigma'}\hat{c}_{i,\mu,\sigma}^{\dagger}\hat{c}_{j,\nu,\sigma'}^{\dagger}\Big]^{N_e/2}|0\rangle, \tag{15}$$

where $F_{i\mu,j\nu}^{\sigma\sigma'}$ are variational parameters to be determined, N_e is a number of electrons in the system, and $|0\rangle$ refers to the vacuum state. Note that when the summation is narrowed to the case where $\sigma \neq \sigma'$, the so-called antiparallel wave function is realized, which is particularly useful for systems in which the total spin z-component is zero [34].

Before we briefly describe the $\hat{\mathcal{P}}$ and $\hat{\mathcal{L}}$ operators applied in this work, it is suitable to sketch the idea of the sampling scheme. The entire method is founded on the variational principle, i.e.,

$$E_G \leqslant E_T \equiv \frac{\langle\Psi_T|\hat{\mathcal{H}}|\Psi_T\rangle}{\langle\Psi_T|\Psi_T\rangle}, \tag{16}$$

where E_G is the ground-state energy. As VMC operates in real space, $|\Psi_T\rangle$ can be expressed in terms of the expansion in the $\{|x\rangle\}$ basis defined explicitly below

$$|x\rangle \equiv |x_\uparrow\rangle \otimes |x_\downarrow\rangle = \prod_{i,\mu\in x_\uparrow}\hat{c}_{i,\mu,\uparrow}^{\dagger}\prod_{j,\nu\in x_\downarrow}\hat{c}_{i,\nu,\downarrow}^{\dagger}|0\rangle, \tag{17}$$

where $x_\uparrow$ and $x_\downarrow$ refer to the set of occupied spin-up and spin-down states, respectively. Configurations $|x\rangle$ are sampled according to the probability density function $\rho(x) \propto |\langle x|\Psi_T\rangle|^2$ and trial ground state energy E_T is estimated as

$$E_T \approx \frac{1}{M}\sum_{m}^{M}\rho(x_m)\frac{\langle\Psi_T|\mathcal{H}|x_m\rangle}{\langle\Psi_T|x_m\rangle} = \frac{1}{M}\sum_{m}^{M}\rho(x_m)E_T^{\text{loc}}(x_m), \tag{18}$$

i.e., as an average of local energy $E_T^{\text{loc}}(x)$ over an assumed number of samples M. The proper selection of $|\Psi_0\rangle$ is one of the most important steps in the variational ansatz construction. However, disregarding the possibility of inclusion of the so-called back-flow correlations [27] in $|\Psi_0\rangle$, we capture the correlation effects in a standard manner [27,34], i.e., by acting
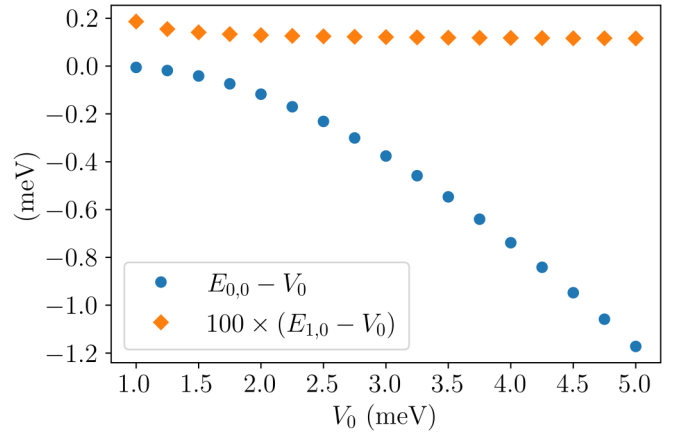

FIG. 2. The ground and the first excited states of isolated QD as a function of V_0. Note that only one bound state exists for the considered range of V_0. The values corresponding to $E_{01} - V_0$ are multiplied by a factor of 100 for clarity.

with a Hermitian operator $\hat{\mathcal{P}}$

$$\hat{\mathcal{P}}\big(\{g_{i\mu}\}, \{v_{i\mu,j\nu}\}, \{\alpha_{n\mu,t\nu}^{d4}, \alpha_{n\mu,t\nu}^{h4}\}\big)$$
$$= \hat{\mathcal{P}}_G(\{g_{i\mu}\})\hat{\mathcal{P}}_J(\{v_{i\mu,j\nu}\})\hat{\mathcal{P}}_{d-h}\big(\{\alpha_{n\mu,t\nu}^{d4}, \alpha_{n\mu,t\nu}^{h4}\}\big) \tag{19}$$

on $|x_m\rangle$.

In the above $\hat{\mathcal{P}}_G$, $\hat{\mathcal{P}}_J$, and $\hat{\mathcal{P}}_{d-h}$ are *Gutzwiller, Jastrow,* and *doublon-holon* correlators, respectively [27,34], and $\{g_{i,\mu}\}$, $\{v_{i\mu,j\nu}\}$, $\{\alpha_{n\mu,t\nu}^{d4}, \alpha_{n\mu,t\nu}^{h4}\}$ are related variational parameters. While $|\Psi_0\rangle$ defined in Eq. (15) explicitly describes a constant number of particles, we also apply the projection on $S_{\text{tot}}^z = 0$ state leading to an antiparallel form of $|\Psi_0\rangle$.

Subsequently, the trial energy E_T can be minimized within the stochastic reconfiguration method, which allows for the efficient optimization with respect to the set of variational parameters [23,32,33]. We perform VMC simulations using a recent, highly efficient, general-purpose package MVMC[34] elaborated by Misawa *et al.*

We also remark that other computational methods suitable for the description of strongly correlated systems may be applied for the solution of the developed interacting Hamiltonian, therefore in the Appendix we provide the values of the computed integrals.

IV. RESULTS

In this section, we first describe the details of the single-particle picture on which the interacting model is founded. Subsequently, we focus on the electronic properties of the system obtained by means of VMC calculations.

A. Single-particle picture

The choice of $r_0 = 20$ nm and $V_0 \in [1.0, 5.0]$ meV provides us with the spectrum of isolated QD containing only a single bound state $\Theta_{0,0}$. The energy levels corresponding to the ground, as well as to the first excited state as a function of V_0 are presented in Fig. 2.

As expected, by changing V_0 we can tune the bound-state energy and as a result modify the band structure of the QD
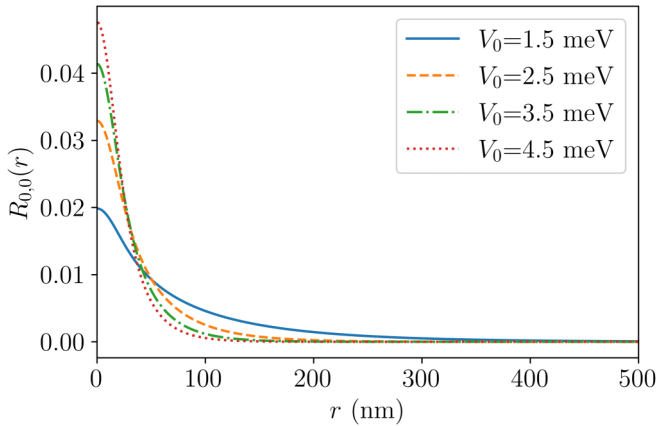
FIG. 3. The evolution of radial part $R_{00}(r)$ for $r_0 = 20$ nm and selected values of V_0.

FIG. 4. The projection of $w_{00}^{R_{0,0}}(x, y)$—i.e., the radial part of Wannier function—onto the $\hat{\mathbf{x}} - \hat{\mathbf{y}}$ plane for $V_0 = 2.5$ meV.

pattern as well as the strength of electronic interactions as we show explicitly in the following. For the chosen form of the $V_{\mathbf{R}}^{\mathrm{QD}}$ potential, a should be sufficiently larger than r_0 so that the potentials of subsequent QDs are relatively well separated and do not overlap. On the other hand, a has to be adequately small to allow for nonzero electron hopping and the development of an electronic band characterized by the reasonable width. We identify that a being few (four to five) times larger than r_0 fulfills both conditions as legitimated in view of the periodic potential formation, i.e., $V_a^C(m \times a/2, n \times a/2) \approx V_0$ holds. In our calculations, we take $a = 100$ nm and $r_0 = 20$ nm. For such a choice the decay of the radial part of the wave function $R_{0,0}$ is presented in Fig. 3.

The considered quantum dot lattice, where only the lowest band is occupied and thus the number of electrons per QD is limited, is suitable for quantum transport measurements as the high-mobility 2DEG can be realized already for electron densities substantially below $10^{11}/\mathrm{cm}^2$ at $T = 0.3$ K [35].

As one can see from Fig. 3 for larger values of V_0 the decay of $\Theta_{0,0}(\mathbf{r})$ is faster with increasing r. It is unknown *a priori* what is the reasonable cutoff for $\mathbf{r_Z}$ in Eq. (6). We find that $Z \lessgtr 5$ should be considered as suitable choice for systems with $V_0 \gtrsim 2$ meV, i.e., for those for which the stronger correlation regime is expected. On the other hand for the weaker confinement the $\mathbf{r_Z}$ cutoff has to be significantly expanded. This observation is natural since for $V_0 \to 0$ the system reduces to a 2DEG with no QD confinement potentials in the $\hat{\mathbf{x}}$–$\hat{\mathbf{y}}$ plane, thus a highly delocalized basis has to be utilized.

In Figs. 4 and 5 we show $w_{0,0}^{R_{00}}$ for $V_0 = 2.5$ meV as an example. One finds that the function is well localized in the vicinity of the central lattice site. However, local extrema are also present (see Fig. 5), which correspond to $\mathbf{r} = (a, 0)$, $\mathbf{r} = (a, a)$ and $\mathbf{r} = (2a, 0)$, i.e., to the first-, second-, and the third-nearest neighbor QDs, respectively. The more distant extrema are below the numerical resolution. Subsequently, we validate the entire procedure by inspecting the orthogonality condition given in Eq. (8), i.e., by computing $\langle \widetilde{w}_{00}^{R_{00}} | \widetilde{w}_{00}^{R_{00}+r_{ij}} \rangle$, where $\mathbf{r}_{ij}$ are vectors pointing to the neighboring sites up to the fifth-nearest neighbor. All the numerical integrations presented in this paper were carried out with the use of the Cuba
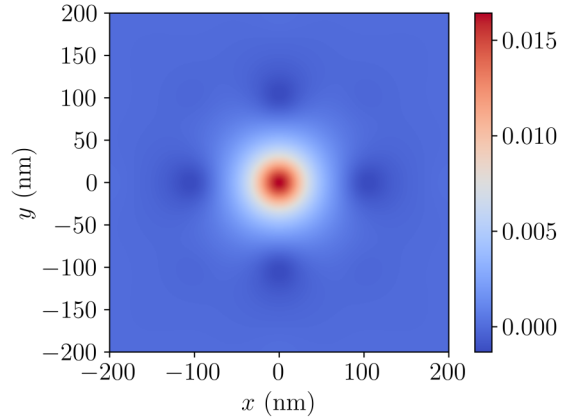
library [36]. The orthogonality discrepancy does not exceed the value of $\propto 10^{-4}$, which we also estimate as the numerical accuracy of Wannier function overlap integrals. Therefore, we find the construction of the Wannier basis as well founded.

Next, we compare the dispersion relations $\epsilon(\mathbf{k})$ for the noninteracting system, resulting from our Wannier basis, with those computed directly from numerical diagonalization of the Schrödinger equation for a QD layer within the KWANT package [37]. Obviously, such a calculation is also biased, e.g., by the finite mesh density. We consider a discrete computational mesh 100 nm × 100 nm with discretization constant $\Delta a = 1$ nm containing a single QD. The mesh is than periodically repeated, effectively describing a translationally invariant, two-dimensional QD lattice. We find very good agreement between both approaches as shown in Fig. 6 where the bare dispersion relations $\epsilon(\mathbf{k})$ are plotted for the representative set of V_0. As supposed, small albeit still noticeable differences are present for $\mathbf{k} = (0, 0)$, i.e., for the Γ point in the momentum space. As one can see for the stronger confinement an indirect gap opens in the band structure. For $V_0 = 2.5$ meV the gap is about 0.5 meV and increases with increasing V_0.
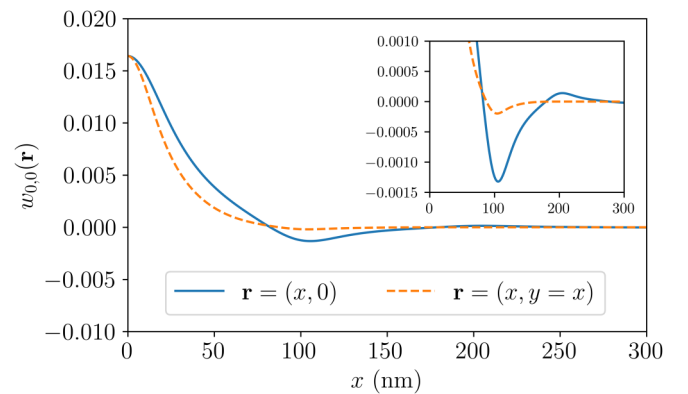

FIG. 5. Wannier states $w_{0,0}^{R_{00}}$ obtained for $V_0 = 2.5$ meV and $a = 100$ nm as a function of $\mathbf{r} = (x, 0)$ and $\mathbf{r} = (x, y = x)$. Well-defined local extrema are visible in the vicinity of location of the nearest, second, and third nearest sites as shown in the inset.
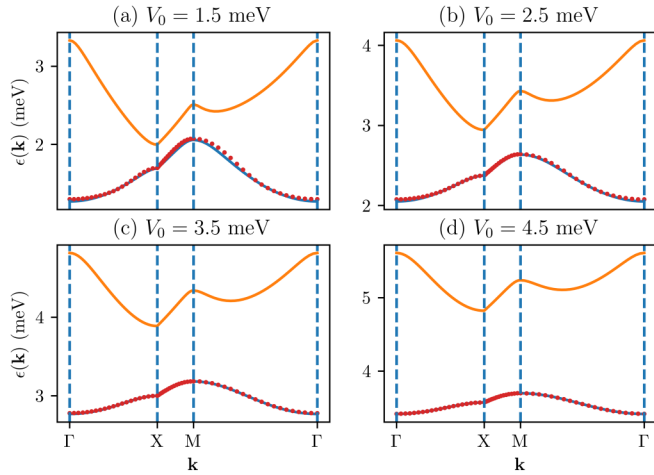
FIG. 6. Bare dispersion relations $\epsilon(\mathbf{k})$ resulting from the first two lowest-lying bands for the selected values of the confinement potential. The lower bands refer to the constructed Wannier basis (symbols) matching the results obtained numerically for the translationally invariant QD lattice (solid blue lines). Also the band-gap enhancement between the first two lowest bands with increasing value of V_0 is noticeable.

For the sake of completeness, in Fig. 7 we present the values of hopping integrals for the considered range of V_0. We relabel each calculated integral $t^{00}_{i(Z),j(Z)} \equiv t_Z$, in such a way that the pair (i, j) of lattice sites correspond to the Zth nearest neighbor. Namely, for $Z \leqslant 5$ the sets of corresponding vectors $\mathbf{R}_{ij}$ which connect the i-site with j-site are given as

$$Z = 1 : \mathbf{R}_{ij} \in \{(\pm a, 0), (0, \pm a), \}, \tag{20a}$$

$$Z = 2 : \mathbf{R}_{ij} \in \{(\pm a, \pm a), (\mp a, \pm a)\}, \tag{20b}$$

$$Z = 3 : \mathbf{R}_{ij} \in \{(\pm 2a, 0), (0, \pm 2a)\}, \tag{20c}$$

$$Z = 4 : \mathbf{R}_{ij} \in \{(\pm 2a, \pm a), (\mp 2a, \pm a),$$
$$(\pm a, \pm 2a), (\mp a, \pm 2a)\}, \tag{20d}$$

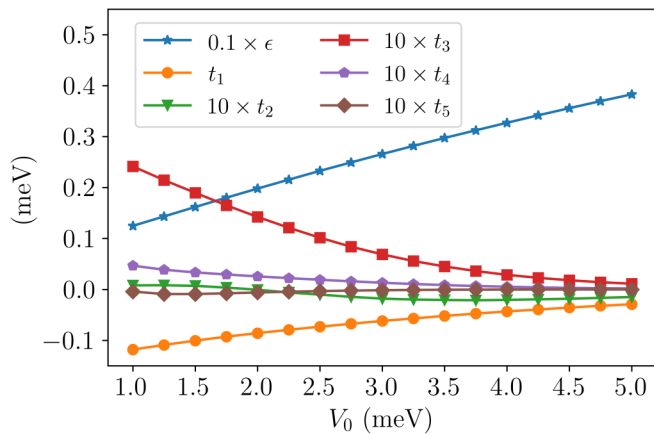$$Z = 5 : \mathbf{R}_{ij} \in \{(\pm 2a, \pm 2a), (\mp 2a, \mp 2a)\}. \tag{20e}$$

FIG. 7. The evolution of hopping integrals as a function of V_0. Note that the value referring to ϵ is divided by a factor of 10, whereas values of t_Z related to $Z > 1$ are multiplied by the same factor for the sake of clarity.
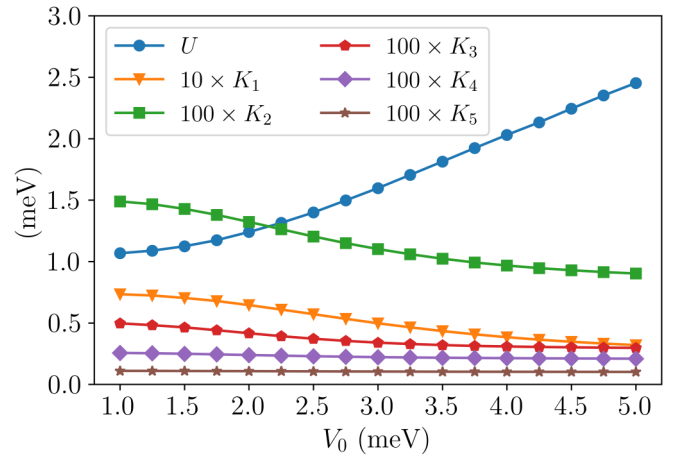

FIG. 8. Density-density interactions as a function of V_0 for $d = 10$ nm. The dominant role of intrasite Hubbard interaction U is clearly evidenced.

The absolute value of the hopping integral to the nearest neighbor is the dominant one, as expected. The characteristic hopping energies correspond to temperatures $|t_1|/k_B \sim 0.1 - 1$K (for $V_0 \sim 1$–3.5 meV), which are reachable by the modern dilution refrigerators. The hoppings referring to the more distant neighbors are substantially smaller (c.a. $\times 10$). We find $|t_3| > |t_2|$ for the entire considered range, and $|t_4| > |t_2|$ for $V_0 \gtrsim 3$ meV. This can be caused by the particular choice of the gauge implicitly encoded in the adopted procedure for the generation of Wannier basis. Notably, the obtained Wannier basis reproduces the band structure obtained directly in momentum space (cf. Fig. 6).

Moreover, as one may deduce from Fig. 7, for $Z > 0$ all amplitudes of hopping integrals taken into account decay with increasing V_0. It is a natural consequence of the stronger localization of Wannier functions with increasing planar confinement. Finally, the role of t_5 is marginal—its absolute value does not exceed 6×10^{-4} meV.

B. Electronic interactions and many-particle Hamiltonian

Whereas the single-particle energy spectrum for a given value of L is only shifted by the ground-state energy of infinite confinement in the $\hat{\mathbf{z}}$ direction, it is not the case for the interaction amplitudes defined in Eq. (12). Furthermore, the thickness of the spacer layer d impacts the magnitude of electronic interactions and can be regarded as a parameter to be tuned in the experimental setup [18].

In Figs. 8–10 we present the values of two-center interactions obtained for $d = 10$ nm. We use the following notations for each type of integrals, omitting band labels, since we consider only a single lowest lying band as presented above. Namely, we define

$$V_{iiii} \equiv U, \tag{21a}$$

$$V_{ijij} \equiv K_{ij}, \tag{21b}$$

$$V_{iijj} = V_{ijji} \equiv J_{ij}, \tag{21c}$$

$$V_{ijjj} = V_{jijj} = V_{jjij} = V_{jjji} \equiv V_{ij}. \tag{21d}$$
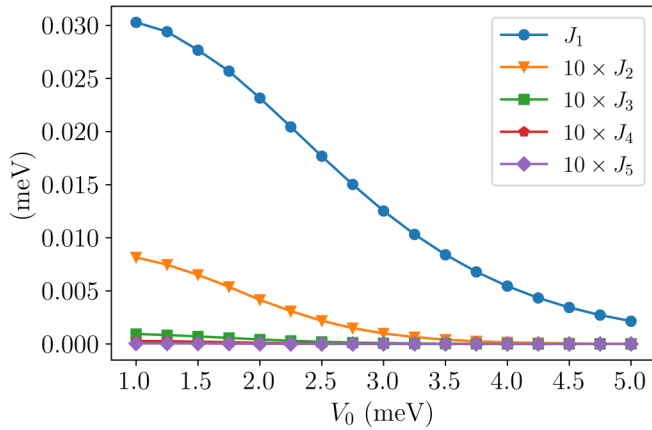
FIG. 9. Exchange integral amplitudes J as a function of V_0 obtained for the screening parameter $d = 10$ nm. All values are positive and therefore refer to the tendency of ferromagnetic order.

One identifies U as the onsite Coulomb repulsion (the so-called Hubbard term), whereas K_{ij} are density-density intersite Coulomb interactions. The exchange-type interactions J_{ij}, as well as the so-called correlated-hopping terms V_{ij}, are invariant under the index exchange due to the fact that the obtained Wannier functions are real. We also follow the nomenclature defined for one-body integrals [see Eq. (20)] e.g., K_1 refers to the density-density interaction between the nearest-neighboring QDs.

As we find that the values of three- and four-center interaction integrals are $\lesssim 10^{-3}$ meV, i.e., close to the estimated numerical precision, we disregard their analysis and exclude them from the final form of the interacting Hamiltonian. However, their role can be regarded as quantitatively influential for multiband models as it has been evidenced for isolated QD-like systems [26].

In Fig. 8 we present the values of K_Z up to $Z = 5$, where we follow the convention assumed also for hopping integrals, e.g., $K_{i(Z),j(Z)} = K_Z$. As expected, the value of U increases with the increasing depth of the confinement potential, becoming dominant for deep potentials. The density-density interaction
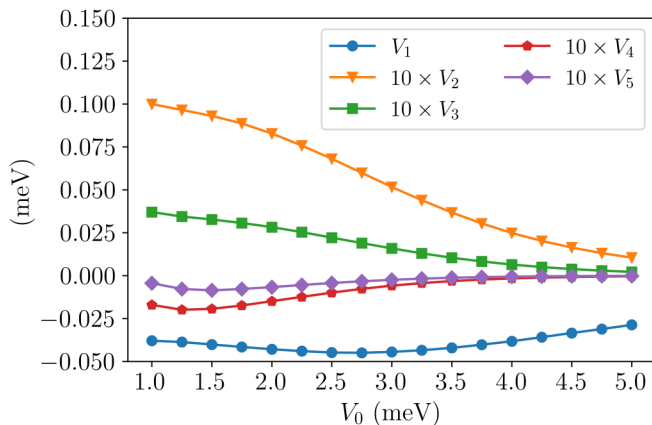

FIG. 10. Correlated-hopping amplitudes as a function of V_0 for $d = 10$ nm. Note that $|V_1|$ is of order of K_1 and its dependence on the gate potential value is nonmonotonical in the considered range of V_0.
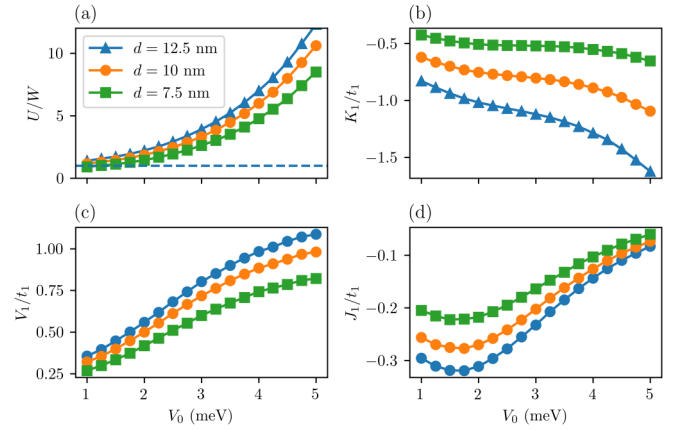

FIG. 11. Relations between electron-electron interaction magnitude and kinetic ingredient for the three different regimes of screening tuned by value of d. The ratio between U and bare dispersion bandwidth (a) $W \equiv \epsilon(\mathbf{k})_{\max} - \epsilon(\mathbf{k})_{\min}$; (b) charge density-density K_1 related to t_1; (c,d) correlated hopping V_1 and exchange interaction J_1 divided by t_1, respectively. The dashed line in (a) relates to $U/W = 1$, i.e., the conventional limit of strong correlations regime.

amplitudes gradually decay as the height of the barrier between QDs is increased. Note that K_1 is of the order of $|t_1|$, therefore intersite interactions are nonnegligible and the system has to be described with the use of the Hamiltonian, which is more complex than that related to pure Hubbard model. The exchange integrals are positive (see Fig. 9), thus indicating the tendency for a ferromagnetic ordering. J_1 is the dominant one and J_Z for $Z > 1$ do not exceed $\sim 10^{-3}$ meV therefore they may be considered as insignificant.

The last type of two-center interactions are correlated hoppings V whose values are presented in Fig. 10. Intriguingly, $|V_1|$ is of the order of magnitude of K_1 and does not behave monotonically in the considered range of V_0. Namely, it attains a minimum $V_1 \approx -0.05$ meV for $V_0 \approx 2.75$ meV. The lack of monotonicity is also present for V_4 and V_5, however, their values are orders of magnitude smaller than V_1.

Whereas the parameter d which tunes the screening effect, does not influence the kinetic energy landscape, it changes the magnitude of interactions. Notably, the relation between electron-electron amplitudes and kinetic energy scale governs the role of electronic correlations in the system. In Fig. 11(a) we depict the conventional measure of correlation strength, which is the ratio between on-site U Hubbard term and a bare dispersion relation width W. One finds that for the considered values of V_0 this ratio systematically grows with the depth of the confinement potential and from this point of view a wide range of strong correlation regimes is accessible in the system. Furthermore, the impact of screening is relatively small when compared to the ratio between density-density interactions K_1 and hopping t_1 [Fig. 11(b)]. For $1.5 \lesssim V_0 \lesssim 4.5$ meV a plateau appears, which becomes less prominent with decreasing value of d. Nevertheless, each depicted value of d provides the magnitude of ratio $|K_1/t_1| \gtrsim 0.5$. This observation suggests that these types of interactions should be taken into account in the many-body interacting Hamiltonian. Although the absolute values referring to the analogous ratios defined for the

correlated hopping and exchange amplitudes [see Figs. 11(c) and 11(d)] are substantially smaller, specifically for lower values of V_0, they still can be regarded as meaningful at least for $Z = 1$. Moreover, they depend more weakly on d as compared to K_1/t_1.

As the decay of K, V, and J with increasing r_Z is of different rate, and, it is *a priori* difficult to state which terms in Hamiltonian can be safely neglected (especially for such a subtle phenomenon as the superconducting pairing), we decided to include all the two-center terms up to $Z = 5$. This choice rather overestimates the role of more distanced (i.e., for $Z > 1$) interaction amplitudes of V and J, however, it allows reducing the doubts concerning the role of each type of interaction in the final picture. Eventually, we analyze the Hamiltonian of the form

$$\hat{\mathcal{H}}_{QDL} = \hat{\mathcal{T}} + \hat{\mathcal{U}} + \hat{\mathcal{K}} + \hat{\mathcal{V}} + \hat{\mathcal{J}}, \tag{22}$$

where $\hat{\mathcal{T}}$ are one body-terms and, $\hat{\mathcal{U}}$, $\hat{\mathcal{K}}$, $\hat{\mathcal{V}}$, and $\hat{\mathcal{J}}$ refer to the two-body interaction terms corresponding to U, K, V, and J, respectively, for the neighboring sites corresponding to $Z \leqslant 5$.

Here, we intend to focus on an experimental setup which potentially may reproduce electronic properties similar to those observed in the typical strongly correlated materials, i.e., the emergence of antiferromagnetic (AF) order, charge gap development for the half-filled band, and finally the creation of superconducting pairing for the doped cases. Whereas the conventional prerequisite for a strong correlation, i.e., U/W is $\gtrsim 1$, is already realized in the system, the relations between other interactions and hopping terms may still play an important role.

Notably, the ferromagnetic interaction J_1 may overcome the AF tendency. This tendency is an inherent feature of the repulsive Hubbard model at half filling as it can be transformed to the t–J model when double occupancies are projected out [7]. Therefore, before selecting the set of microscopic parameters to be applied for the variational solution of our Hamiltonian, we carried out the following reasoning. The inclination for AF ordering close to half-filling can be estimated by comparing the coupling $J_{t-J} = 4t^2/U$ derived for the t–J model and the value of the ferromagnetic exchange integral, J_1. As shown in Fig. 12, such an estimation suggests that when *screening* is enhanced, i.e., d decreases, the antiferromagnetic order can be expected to dominate. Note also, that $d < L/2$ must hold to satisfy the consistency of model. For $d = 7.5$ nm the thickness of layer below the pattern of electrodes which is not penetrated by electrons from 2DEG is still 2.5 nm.

Moreover, the pair-hopping term associated with J_1 can lead to Cooper pair modulation of the on-site s-wave paired state [38]. However, in the regime of relatively large on-site repulsion U the intersite paired state is much more likely to be expected. The mentioned mechanism of inducing the Cooper pair modulation is not going to be operative in such a case of intersite pairing. Thus, we turn to a detailed investigation of the homogeneous intersite paired state.

Finally, we consider the general Hamiltonian given in Eq. (22) for $d = 7.5$ nm and $V_0 \in [2.0, 4.0$ meV], which we suspect have properties similar to those of the descendants of the repulsive Hubbard model in the strong correlation regime.
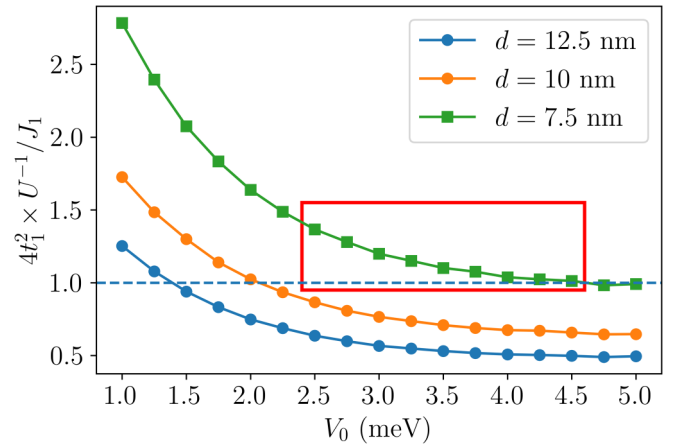

FIG. 12. The relation $(4t_1^2/U)/(J_1)$ as a function of V_0. The dashed horizontal line separates estimated applicability of Hubbard/t − j (upper) and ferromagnetic Heisenberg (lower) models close to the half-filling. The red rectangle surrounds cases considered in our VMC calculations.

C. VMC solution for the interacting system

As mentioned in Sec. II the variational ansatz employed in this work can be regarded as highly generic, i.e., capable of describing a variety of complex phases. However, as it is a challenging task from the optimization perspective, even for the less complex model Hamiltonians, we exclude the possibility of long-range charge ordering in our analysis assuming a 1×1 variational parameters sublattice [34]. Nevertheless, the adopted form is flexible enough to cover singlet s- and d-wave pairing as well as antiferromagnetic spin ordering. Namely, we do not impose any rotational symmetry for $F_{ij}^{\uparrow\downarrow}$ and *Jastrow*-type variational parameters. Also, as we consider a single-band model, the final set of variational parameters is augmented with the single *Gutzwiller* projector parameter g, as well as, with ten parameters associated with local electron occupancy configurations supplying single *doublon-holon* correlator.

For a lattice consisting of $N_x \times N_y$ sites the number of variational parameters scales as the number of considered QDs since the pattern of connections between sites is repeated for each site, eventually forming a translationally invariant scheme.

1. Spin-spin correlation functions and charge gap

As stated, we are mainly interested if the considered system exhibits properties characteristic for strongly correlated systems such as cuprates. Namely, we expect that for the half-filled band, AF ordering should appear. The analysis of the magnetic properties was carried out by calculating the correlation functions defined for the spin z-component as

$$S^z(\mathbf{r}) = \frac{1}{N_x \times N_y} \sum_i \langle (\hat{n}_{i\uparrow} - \hat{n}_{i\downarrow})(\hat{n}_{f(\mathbf{R_i}+\mathbf{r})\uparrow} - \hat{n}_{if(\mathbf{R_i}+\mathbf{r})\downarrow}) \rangle,$$
$$\tag{23}$$

where function $f(\mathbf{r})$ maps vector $\mathbf{r}$ onto the proper lattice index. Also, we consider correlation functions defined in the momentum space which are Fourier transforms of their real-
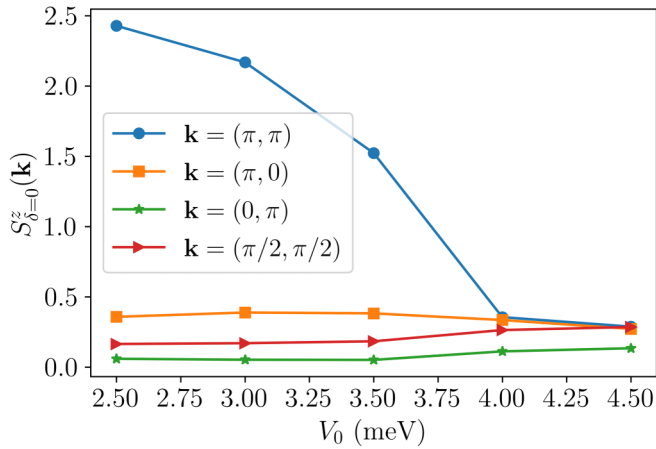
FIG. 13. Momentum-resolved spin-spin correlation functions for the representative values of **k** at $\delta = 0$ as a function of V_0 for the system consisting of 8×8 QDs.
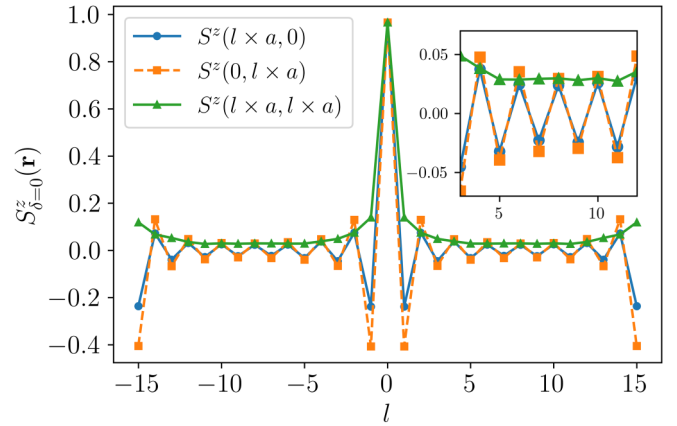

FIG. 14. Real-space spin-spin correlation functions at $\delta = 0$, for $V_0 = 3$ meV and lattice consisting of 16×16 QDs. The discrepancy between $\hat{\mathbf{x}}$ and $\hat{\mathbf{y}}$ directions is observed, however, this difference decays with increasing $|l|$. The statistical error is smaller than the symbol's size.

space counterparts $S^z(\mathbf{r})$, i.e.,

$$S^z(\mathbf{k}) = \sum_j e^{i\mathbf{k} \cdot \mathbf{R}_j} S^z(\mathbf{R}_j). \tag{24}$$

First, we intend to verify if our conjectures regarding the AF ordering at half-filling for the selected range of V_0 and $d = 7.5$ nm are valid. Therefore, we performed preliminary calculations for the system of size 8×8 and for doping $\delta = 0$, where

$$\delta = 1 - \frac{N_{el}}{N_x \times N_y}. \tag{25}$$

To reduce the finite-size effects, we imposed periodic boundary conditions on the lattice.

The resulting evolution of $S^z(\mathbf{k})$ with V_0 for different magnetic modulation vectors is presented in Fig. 13. It is clearly visible that the antiferromagnetic type of spin ordering dominates for $2.5 \lesssim V_0 \lesssim 3.5$ meV. Already here we can see that the ground-state magnetic properties of the system can be tuned by changing the gate potential V_0.

In Fig. 14 we show how the spin-spin correlation function changes in real space along the (1,0), (0,1), and (1,1) directions of the QD square lattice for a larger system (16×16) and for the gate potential $V_0 = 3$ meV. In agreement with the results presented in Fig. 13 we observe the behavior characteristic for the AF ordering. It should be noted that small differences between the (1,0) and (0,1) directions are visible in Fig. 14 in spite of the fact that the system itself is C_4 symmetric. Such a spontaneous symmetry breaking is possible since the exploited variational ansatz is not constrained to be symmetric with respect to the spatial directions. Despite these circumstances, the AF ordering is strongly manifested. In addition, the (1,0)/(0,1) asymmetry decreases with increasing distance as well as it weakens as the system becomes larger. Therefore, the observed C_4 symmetry breaking can vanish in the thermodynamic limit for the considered variational ansatz.

For the sake of completeness in Fig. 15 we present $S^z(\mathbf{k})$ as a function of both electron and hole doping $\delta \in [-0.5, 0.5]$ for $\mathbf{k} \in \{(\pi, \pi), (0, \pi), (\pi, 0), (\pi/2, \pi/2)\}$. As expected, AF ordering dominates. For one electron per single QD, a well-

pronounced peak emerges and the values corresponding to the remaining directions are marginal.

The appearance of the AF ordering close to the zero-doped case is typical for the family of copper-based high-temperature superconductors [2]. For the later systems, the (π, π) magnetic modulation is accompanied by the electron-electron interaction-induced insulating state. Therefore, here we also analyze the possibility of charge gap creation which is a signature of the Mott insulator. For this reason, we calculate the approximate value of the chemical potential

$$\mu(\delta) \approx \frac{E(N_{el}) - E(N_{el} - \Delta N_{el})}{\Delta N_{el}}, \tag{26}$$

which allows us to determine the value of the charge gap in the following manner:

$$\Delta_{CG} = \lim_{\delta \to 0^-} \mu(\delta) - \lim_{\delta \to 0^+} \mu(\delta). \tag{27}$$

In Fig. 16 we present $\mu(\delta)$ for 16×16 QD lattice within resolution $\Delta N_{el} = 8$. An abrupt change of the chemical potential
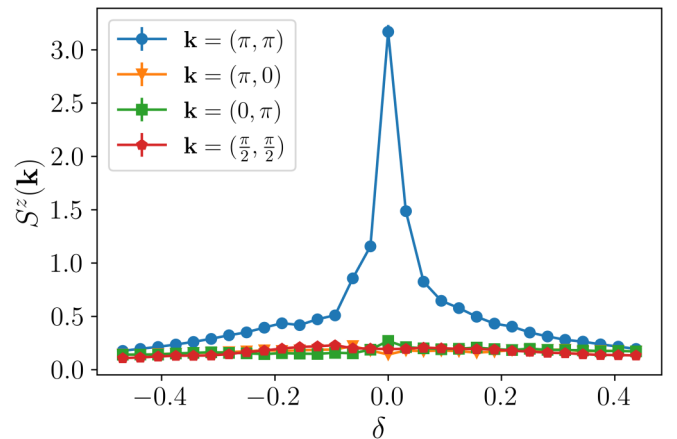

FIG. 15. Momentum space spin-spin correlation functions for $V_0 = 3$ meV and lattice consisting of 16×16 QDs as a function of doping.
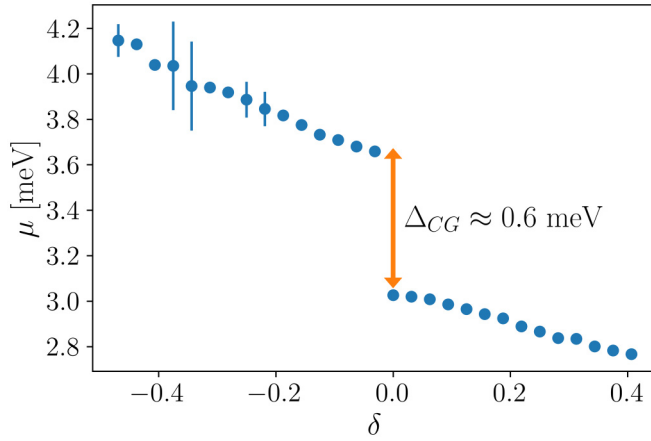
FIG. 16. Estimated chemical potential μ as a function δ. The arrow represents the resulting charge-gap estimation. In most cases, errors are smaller than the symbol size.

FIG. 17. Pairing $\overline{P}_q$ at maximal possible distance $\mathbf{R}_{max}$ for 8×24 QD lattice as a function of doping. Dashed horizontal line refers to van Hove singularity obtained for the noninteracting system.

for $\delta = 0$, resulting in $\Delta_{CG} \approx 0.6$ meV indicates an insulating character of the system. Since in our case the Hubbard interaction is $U \approx 1.2$ meV and the bandwidth is $W \approx 0.45$ meV, the simplest estimate of the charge gap for the case of the Hubbard model can be given roughly as $\Delta_{CG} = U - W \approx 0.75$ meV—a value which is close to the one obtained here. We find that the principal features of the considered system are determined by the intrasite repulsion together with the form of band structure, which is the case known from the Hubbard model.

It should be noted that in general the intersite Coulomb repulsion terms may induce the insulating state at the $\delta = \pm 0.5$ dopings and/or the charge ordered states. However, as shown in Fig. 8, the intersite Coulomb repulsion integrals are relatively small in the considered parameter range. Therefore, the mentioned effects are not expected here.

Another prominent phenomenon related to the physics of strongly correlated systems is the formation of the superconducting state upon electron or hole doping. The appearance of superconductivity in the considered system is analyzed in the following subsection.

Since even for the pure Hubbard model, the full phase diagram is not indisputably settled [6,39], one may expect that for the more complex Hamiltonian considered here, a variety of charge and spin ordered states should be put under examination. This is, however, beyond the scope of the present study, which focuses on *archetypal* properties of strongly correlated systems in view of Hubbard-like models.

2. Pairing correlation functions

We analyze the possibility of singlet pairing by considering the pair correlation functions defined in the following manner:

$$P_q(\mathbf{R}_{ij}) = \sum_{\mathbf{a},\mathbf{a}'} g_q(\mathbf{a}) g_q(\mathbf{a}') \langle \hat{\Delta}_{i,f(\mathbf{R_i}+\mathbf{a})}^{\dagger} \hat{\Delta}_{j,f(\mathbf{R_j}+\mathbf{a}')} \rangle, \quad (28)$$

where q stands for pairing channel (d or s), $\mathbf{a}$ ($\mathbf{a}'$) is the $(\pm a, 0), (0, \pm a)$ vector, and $g_q(\mathbf{a})$ is the symmetry-related factor which takes the form $g_s(\mathbf{a}) = g_d(\pm a, 0) = -g_d(0, \pm a) = 1$. The singlet-pairing operators $\hat{\Delta}_{ij}^{\dagger}$ are
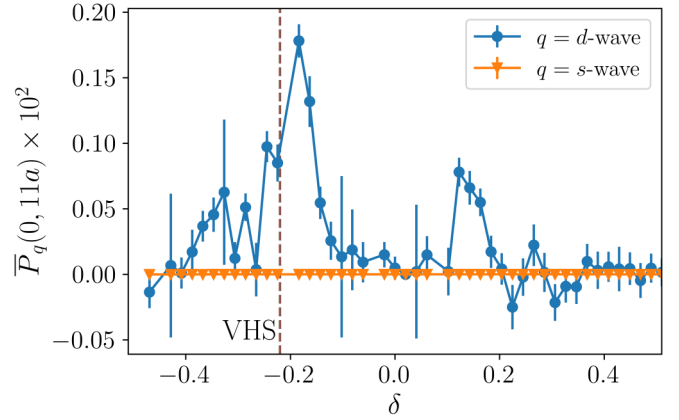
defined as

$$\hat{\Delta}_{ij}^{\dagger} = \frac{1}{\sqrt{2}}(\hat{c}_{i\uparrow}^{\dagger} \hat{c}_{j\downarrow}^{\dagger} - \hat{c}_{i\downarrow}^{\dagger} \hat{c}_{j\uparrow}^{\dagger}). \quad (29)$$

As the tendency for pairing should be analyzed for $\lim_{|\mathbf{R}_{ij}| \to \infty} P_q(\mathbf{R}_{ij})$, which cannot be realized in practice for a finite lattice, nonzero values of $P_q(\mathbf{R}_{ij})$ can be falsely interpreted as signatures of the superconducting state [40]. To overcome this difficulty, we compute the vertex pairing functions [40–43] given as

$$\overline{P}_q(\mathbf{R}_{ij}) = P_q(\mathbf{R}_{ij}) - \sum_{\mathbf{a},\mathbf{a}'} g_q(\mathbf{a}) g_q(\mathbf{a}')$$

$$\times [\langle \hat{c}_{i\uparrow}^{\dagger} \hat{c}_{j\uparrow} \rangle \langle \hat{c}_{f(\mathbf{R_i}+\mathbf{a})\downarrow}^{\dagger} \hat{c}_{f(\mathbf{R_j}+\mathbf{a}')\downarrow} \rangle$$

$$+ \langle \hat{c}_{i\uparrow}^{\dagger} \hat{c}_{\mathbf{R_j}+\mathbf{a}'\uparrow} \rangle \langle \hat{c}_{f(\mathbf{R_i}+\mathbf{a})\downarrow}^{\dagger} \hat{c}_{j\downarrow} \rangle$$

$$+ \langle \hat{c}_{i\downarrow}^{\dagger} \hat{c}_{j\downarrow} \rangle \langle \hat{c}_{f(\mathbf{R_i}+\mathbf{a})\uparrow}^{\dagger} \hat{c}_{f(\mathbf{R_j}+\mathbf{a}')\uparrow} \rangle$$

$$+ \langle \hat{c}_{i\downarrow}^{\dagger} \hat{c}_{\mathbf{R_j}+\mathbf{a}'\downarrow} \rangle \langle \hat{c}_{f(\mathbf{R_i}+\mathbf{a})\uparrow}^{\dagger} \hat{c}_{j\uparrow} \rangle]. \quad (30)$$

The subtraction of the products of the hopping averages allows finding a reliable estimation of the tendency for the pairing in the finite-size system [40]. We obtain the vertex functions for $\mathbf{R}_{ij}$ oriented along $\hat{\mathbf{x}}$ for $V_0 = 3$ meV, $d = 7.5$ nm and for the lattice size $L_x \times L_y = 8 \times 24$. In Fig. 17 we present $\overline{P}_q$ for both d- and s-wave pairing symmetries as a function of doping δ, calculated for $R_{max} = (0, 11a)$. As the pairing amplitude in general is relatively small and may be affected by statistical noise, the averaging procedure is performed within $\sim 10^8$ Monte Carlo steps and repeated ten times for each considered doping to estimate the statistical error.

As shown in Fig. 17 a dome-like behavior for the d-wave amplitude appears in the electron-doped region of the phase diagram. Namely, nonzero vertex pairing functions are obtained for $-0.37 \lesssim \delta \lesssim -0.12$, as well as for the hole-doped case $0.1 \lesssim \delta \lesssim 0.18$. The later case exposes a noticeable smaller amplitude than the first and poses a less smooth shape. Nevertheless, both doping regimes show a clear tendency towards the superconducting phase formation within the d-wave pairing channel.
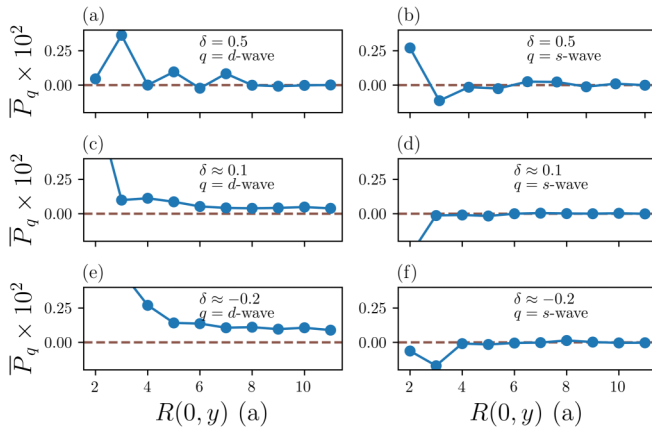
FIG. 18. Pairing $\overline{P}_q$ as function of distance $R(0, y)$ for 8×24 QDL for the selected values of doping δ.

In Fig. 18 the spatial dependency of $\overline{P}_q$ is shown for three representative cases. We find that the chosen system dimensions allow capturing the asymptotic tendency. Namely, for $R(0, y) \gtrsim 8$ pairings related to d-wave channel converge within the estimated statistical error. The s-wave pairing vertex function decays to the value close to zero even more rapidly, i.e., for $R(0, y) \gtrsim 4$ only the residual values are observed. Furthermore, we disregard the analysis of inconclusive cases, i.e., those for which related statistical errors and/or values are greater of the order of magnitude than those exhibited by majority.

The two peaks related to the d-wave pairing regions separated by the AF phase resemble the phase diagram identified for the cuprate superconductors. However, in our case, the paired state is more pronounced at the electron-doped site instead of the hole-doped situation. This can be understood in view of the so-called van Hove singularity scenario [44] according to which the peak in the density of states for the layered structures has a significant influence on the enhancement of the paired state regardless of the particular pairing mechanism. Although the Bardeen-Cooper-Schrieffer (BCS)-type mechanism is not often discussed in view of the cuprate physics and is surely absent in the QD lattice analyzed here, the peak in the density of states may also influence the correlation-driven pairing as it is suggested in [45]. Since for the cuprates the van Hove singularity is reached at the hole-doped site of the phase diagram, the superconducting dome is more pronounced for $\delta > 0$. On the other hand, for the case analyzed here, the bare band-structure calculations reveal the singularity at $\delta \approx -0.22$, i.e., inside the electron-doped regime. As shown in Fig. 17, this value coincides with the doping range for which the obtained amplitudes of d-wave pairing are characterized by the largest magnitude. Additionally, close to $\delta = 0$ the emergence of AF state appears (see Fig. 15) together with the Mott insulating state, which leads to the suppression of the paired state in the close proximity of half-filling and leaving an asymmetric two-dome structure of the superconducting pairing amplitudes.

Finally, as shown the *d-wave* symmetry dominates over the *extended s-wave* pairing in the considered doping range. This fact comes as a result of the relative position of the Fermi surface and the nodal lines corresponding to the

particular symmetry factor. The symmetry that results in less suppression of the superconducting gap at the Fermi surface is chosen by the system as it makes the paired state more stable. The obtained result is in agreement with the previous calculations made for the simple Hubbard model where the d-wave symmetry is also stable in the range around the half-filled situation [46].

V. SUMMARY

We developed a model describing the QD lattice and numerically analyzed the electronic characteristics in the strongly correlated regime within the low carrier density regime.

We showed that the system can be described by a single band of interacting electrons. We found that, by properly tuning the gate potential, we can reach the situation in which the width of the band is relatively small when compared to the electron-electron interaction amplitudes and thus making the properties of the system dominated by electronic correlations. Furthermore, by estimating the antiferromagnetic coupling within the approach based on the t-J model we found that the inherent correlation-driven effective antiferromagnetic ordering can overcome the trend of ferromagnetic spin alignment.

The variational Monte-Carlo simulations for the obtained model showed that the QD lattice exhibits three main features of strongly correlated high-temperature superconductors: (i) tendency towards AF ordering when the charge density is close to one electron per QD; (ii) development of charge gap which can be related to the Mott insulating state; and (iii) emergence of the d-wave pairing which exhibits a two-dome structure. We found that the pairing is stronger in the electron-doped regime, in contrast to the situation observed in cuprates. This can be related to the character of the bare band structure, which exhibits a peak in the density of states for the case of electron-doped case.

Therefore, one may conclude that the main features of the system under consideration qualitatively resemble those known from cuprates, rendering such a QD lattice as an experimentally accessible, electrically tunable, artificial material that would allow studying the physics of correlated systems.

The code and the data behind the presented figures can be downloaded from an open repository together with the values of the adopted microscopic parameters [47].

APPENDIX: MICROSCOPIC PARAMETERS FOR THE INTERACTING HAMILTONIAN

In this Appendix we provide values of microscopic parameters up to $Z = 5$ for $V_0 = 3.0$ meV and $d = 7.5$ nm, i.e., for the system for which the analysis of magnetic as well as pairing properties has been carried out for the interacting Hamiltonian (see Tables I–IV). An estimated error is $\propto 10^{-4}$.

TABLE I. Values of single-particle parameters; note that $\epsilon \equiv t_0$.

Single-particle parameters (meV)					
ϵ	t_1	t_2	t_3	t_4	t_5
2.657	-0.061	-0.002	0.007	0.001	0.000

TABLE III. Values of exchange interaction amplitudes.

Exchange interactions (meV)					
J_1	J_2	J_3	J_4	J_5	
0.010	0.000	0.000	0.000	0.000	

TABLE II. Values of Coulomb density-density interaction amplitudes, here $U \equiv K_0$.

Density-density Coulomb interactions (meV)					
U	K_1	K_2	K_3	K_4	K_5
1.262	0.032	0.006	0.002	0.001	0.001

TABLE IV. Values of correlated hopping interaction amplitudes.

Correlated hoppings interactions (meV)					
V_1	V_2	V_3	V_4	V_5	
-0.037	0.004	0.001	0.000	0.000	

[1] M. Imada, A. Fujimori, and Y. Tokura, Rev. Mod. Phys. **70**, 1039 (1998).

[2] M. Ogata and H. Fukuyama, Rep. Prog. Phys. **71**, 036501 (2008).

[3] D. F. Agterberg, J. S. Davis, S. D. Edkins, E. Fradkin, D. J. Van Harlingen, S. A. Kivelson, P. A. Lee, L. Radzihovsky, J. M. Tranquada, and Y. Wang, Annu. Rev. Condens. Matter Phys. **11**, 231 (2020).

[4] F. Steglich, Philos. Mag. **94**, 3259 (2014).

[5] J. Hubbard, Proc. R. Soc. London A **276**, 238 (1963).

[6] M. Qin, T. Schäfer, S. Andergassen, P. Corboz, and E. Gull, The hubbard model: A computational perspective, arXiv:2104.00064.

[7] J. Spałek, Acta Phys. Pol. A **111**, 409 (2007).

[8] Y. Cao, V. Fatemi, A. Demir, S. Fang, S. L. Tomarken, J. Y. Luo, J. D. Sanchez-Yamagishi, K. Watanabe, T. Taniguchi, E. Kaxiras, R. C. Ashoori, and P. Jarillo-Herrero, Nature (London) **556**, 80 (2018).

[9] Y. Cao, V. Fatemi, S. Fang, K. Watanabe, T. Taniguchi, E. Kaxiras, and P. Jarillo-Herrero, Nature (London) **556**, 43 (2018).

[10] T. Esslinger, Annu. Rev. Condens. Matter Phys. **1**, 129 (2010).

[11] W. Hofstetter, J. I. Cirac, P. Zoller, E. Demler, and M. D. Lukin, Phys. Rev. Lett. **89**, 220407 (2002).

[12] S. Tarucha, D. G. Austing, T. Honda, R. J. van der Hage, and L. P. Kouwenhoven, Phys. Rev. Lett. **77**, 3613 (1996).

[13] N. Hendrickx, D. Franke, A. Sammak, M. Kouwenhoven, D. Sabbagh, L. Yeoh, R. Li, M. L. V. Tagliaferri, M. Virgilio, G. Capellini, G. Scappucci, and M. Veldhorst, Nat. Commun. **9**, 2835 (2018).

[14] T. Hensgens, T. Fujita, L. Janssen *et al.*, Nature (London) **548**, 70 (2017).

[15] C. J. van Diepen, T. K. Hsiao, U. Mukhopadhyay, C. Reichl, W. Wegscheider, and L. M. K. Vandersypen, Phys. Rev. X **11**, 041025 (2021).

[16] U. Mukhopadhyay, J. P. Dehollain, C. Reichl, W. Wegscheider, and L. M. K. Vandersypen, Appl. Phys. Lett. **112**, 183505 (2018).

[17] T. Byrnes, N. Y. Kim, K. Kusudo, and Y. Yamamoto, Phys. Rev. B **78**, 075320 (2008).

[18] T. Byrnes, P. Recher, N. Y. Kim, S. Utsunomiya, and Y. Yamamoto, Phys. Rev. Lett. **99**, 016405 (2007).

[19] S. Bednarek, B. Szafran, K. Lis, and J. Adamowski, Phys. Rev. B **68**, 155333 (2003).

[20] M. Ciurla, J. Adamowski, B. Szafran, and S. Bednarek, Physica E **15**, 261 (2002).

[21] V. Laliena and J. Campo, J. Phys. A: Math. Theor. **51**, 325203 (2018).

[22] J. G. Aiken, J. A. Erdos, and J. A. Goldstein, Int. J. Quantum Chem. **18**, 1101 (1980).

[23] A. Biborski, A. P. Kądzielawa, and J. Spałek, Phys. Rev. B **98**, 085112 (2018).

[24] J. Qin, Q. Zhou, B. Liao, and H. Wang, Electronics **7**, 410 (2018).

[25] J. Spałek, E. M. Görlich, A. Rycerz, and R. Zahorbeński, J. Phys.: Condens. Matter **19**, 255212 (2007).

[26] A. Biborski, A. P. Kądzielawa, A. Gorczyca-Goraj, E. Zipper, M. M. Maśka, and J. Spałek, Sci. Rep. **6**, 29887 (2016).

[27] F. Becca and S. Sorella, *Quantum Monte Carlo Approaches For Correlated Systems* (Cambbridge University Press, Cambridge, England, 2017).

[28] J. Toulouse, R. Assaraf, and C. J. Umrigar, in *Electron Correlation in Molecules–ab initio Beyond Gaussian Quantum Chemistry*, Adv. Quantum Chem., Vol. 73, edited by P. E. Hoggan and T. Ozdogan (Academic, New York, 2016), pp. 285–314.

[29] H.-H. Zhao, K. Ido, S. Morita, and M. Imada, Phys. Rev. B **96**, 085103 (2017).

[30] D. Kato and K. Kuroki, Phys. Rev. Research **2**, 023156 (2020).

[31] S. Tamura and H. Yokoyama, Phys. Procedia **81**, 5 (2016), proceedings of the 28th International Symposium on Superconductivity (ISS 2015) November 16–18, 2015, Tokyo, Japan.

[32] M. Zegrodnik, A. Biborski, M. Fidrysiak, and J. Spałek, Phys. Rev. B **99**, 104511 (2019).

[33] A. Biborski, M. Zegrodnik, and J. Spałek, Phys. Rev. B **101**, 214504 (2020).

[34] T. Misawa, S. Morita, K. Yoshimi, M. Kawamura, Y. Motoyama, K. Ido, T. Ohgoe, M. Imada, and T. Kato, Comput. Phys. Commun. **235**, 447 (2019).

[35] Y. J. Chung, K. A. Villegas Rosales, K. W. Baldwin, P. T. Madathil, K. W. West, M. Shayegan, and L. N. Pfeiffer, Nat. Mater. **20**, 632 (2021).

[36] T. Hahn, Comput. Phys. Commun. **168**, 78 (2005).

[37] C. W. Groth, M. Wimmer, A. R. Akhmerov, and X. Waintal, New J. Phys. **16**, 063065 (2014).

[38] J. Wårdh, B. M. Andersen, and M. Granath, Phys. Rev. B **98**, 224501 (2018).

[39] D. P. Arovas, E. Berg, S. A. Kivelson, and S. Raghu, Ann. Rev. Conden. Matter Phys. **13**, (2022).

[40] S. R. White, D. J. Scalapino, R. L. Sugar, E. Y. Loh, J. E. Gubernatis, and R. T. Scalettar, Phys. Rev. B **40**, 506 (1989).

[41] K. Kuroki, Y. Tanaka, T. Kimura, and R. Arita, Phys. Rev. B **69**, 214511 (2004).

[42] S.-C. Fang, G.-K. Liu, H.-Q. Lin, and Z.-B. Huang, Phys. Rev. B **100**, 115135 (2019).

[43] Z. B. Huang, H. Q. Lin, and J. E. Gubernatis, Phys. Rev. B **64**, 205101 (2001).

[44] J. Bok and J. Bouvier, J. Supercond. Nov. Magn. **25**, 657 (2012).

[45] R. Markiewicz, J. Phys. Chem. Solids **58**, 1179 (1997).

[46] J. Kaczmarczyk, J. Spałek, T. Schickling, and J. Bünemann, Phys. Rev. B **88**, 115127 (2013).

[47] A. Biborski, M. P. Nowak, and M. Zegrodnik, Quantum dot lattice in the correlated state - data and charts, Zenodo (2021), doi:10.5281/zenodo.5529809.